

Bioinspired interfacial nanofluidic layer enabling high-rate and dendrite-free lithium metal negative electrodes

Received: 6 September 2024

Accepted: 1 August 2025

Published online: 28 August 2025



Chunlei Song^{1,2,4}, Lyuming Pan^{1,2,4}, Junxiu Wu^{3,4}, Lu Chen¹, He Zhao¹, Hongji Pan¹, Shumin Wu¹, Liu Yang¹, Yanxin Jiang¹, Yiju Li^{1,2}✉, Jun Lu³✉ & Tianshou Zhao^{1,2}✉

Lithium metal negative electrodes are highly promising for high-specific-energy batteries due to their low electrochemical potential and high capacity. However, dendrite growth due to limited Li^+ transport at the interface hinder their performance and safety. Enhancing interfacial Li^+ transport can prevent Li^+ depletion and ensure uniform Li deposition. Herein, an artificial interphase layer inspired by the nanofluidic effects in organisms is developed. The artificial interphase layer exhibits nanofluidic ion transport behavior, offering a 3.6 times higher transference number and a 10^7 times higher diffusion coefficient for Li^+ compared to bulk solutions at a low Li salt concentration of $10^{-6} \text{ mol L}^{-1}$. Such selective Li^+ conduction can effectively suppress dendritic growth, achieving a stable Li plating/stripping cycling at a current density of 200 mA cm^{-2} and a high Coulombic efficiency of 99.7%. Consequently, the negative electrode-free Cu||LFP cell achieves 80.1% capacity retention after 200 cycles. Moreover, the Li||S full cell demonstrates high stability over 300 cycles with a 70.7% capacity retention at -20°C and achieves a high specific energy of 505.1 Wh kg^{-1} with designed capacity of 127.3 mAh (stack level). This nature-inspired interfacial nanofluidic layer design offers a promising strategy for developing high-rate, dendrite-free lithium metal negative electrodes.

With the rapid advancement in energy technologies, commercial lithium-ion batteries (LIBs) struggle to meet the escalating demand for high-energy-density storage devices. Lithium metal negative electrodes (LMEs) are recognized as highly promising candidates for developing high-specific-energy batteries due to their high theoretical capacity (3860 mAh g^{-1})^{1,2}. However, they face significant challenges such as the formation of Li dendrites and substantial volume change during cycling, which often result in low Coulombic efficiency (CE) and severe safety issues, especially at high current densities^{3,4}.

Numerous research endeavors have been dedicated to suppressing Li dendrites through various approaches, including the use of three-dimensional (3D) current collectors, lithiophilic alloys, electrolyte optimization, and the development of artificial solid electrolyte interfaces (SEI)^{5–7}. While 3D structures can mitigate the uncontrolled volume changes during Li stripping and plating, they also increase the contact area, leading to increased side reactions with electrolytes⁸. The formation of Li alloys can effectively guide the nucleation and growth of Li, yet parasitic reactions between electrolytes and Li alloys still seriously affect the battery life⁹. Electrolyte design aimed at facilitating

¹Department of Mechanical and Energy Engineering, Southern University of Science and Technology, Shenzhen, PR China. ²SUSTech Energy Institute for Carbon Neutrality, Southern University of Science and Technology, Shenzhen, PR China. ³College of Chemical and Biological Engineering, Zhejiang University, Hangzhou, PR China. ⁴These authors contributed equally: Chunlei Song, Lyuming Pan, Junxiu Wu. ✉e-mail: lijj6@sustech.edu.cn; junzoelu@zju.edu.cn; zhaots@sustech.edu.cn

in-situ SEI layer formation on Li metal surfaces is an effective strategy for managing the stripping and deposition processes. However, the mechanical robustness of SEI layers is often insufficient to prevent dendrite penetration at high current densities¹⁰. Among these strategies, the utilization of artificial interphase layers is effective in regulating the Li stripping/plating behavior and decreasing the interfacial side reactions^{11,12}. However, the mechanism of how the evolution of ion concentration at the Li metal interface affects the ion transport behavior at the interface layer has not been revealed, and the rate capability of the Li metal functionalized by the artificial interface layers needs to be urgently improved to meet the high-rate practical applications.

The limited transport capability of Li⁺ ions at the interface of Li metal during deposition is a significant factor contributing to the poor rate and cycling performance of LMEs. Sand's formula indicates that in low-concentration electrolytes and under high current densities, a Li⁺ depletion zone easily forms due to inadequate Li⁺ replenishment, forcing Li deposition primarily at the electrode surface tips¹³. Sand's time (T_{sand}), derived from Sand's formula, characterizes Li⁺ transport efficiency and correlates with the onset of Li dendrite growth at these tips^{14–16}. A higher T_{sand} value signifies better Li⁺ transport capability, which is influenced by factors such as electrolyte concentration (C_0), Li⁺ transference number (μ_+), and Li⁺ diffusion coefficient (D). However, when Li plating, the electrolyte concentration at the electrode interface decreases, leading to a reduction in both μ_+ and D of Li⁺, which can promote dendrite formation^{17–19}. Therefore, enhancing the μ_+ and D of Li⁺ at the Li metal interface presents a promising avenue for realizing high-rate rechargeable lithium metal batteries (LMBs).

In organisms, ion regulation is a widespread phenomenon²⁰. Biological ion channels situated across cell membranes play crucial roles in mediating ion communication between the cell interior and the extracellular environment²¹. These ion channels exhibit two distinct characteristics: high ion selectivity and fast ion transmission (ion flux rate reaching up to 10^6 – 10^8 ions per second)²². For instance, in response to an electrical signal in the brain, ion channels facilitate the swift transmission of K⁺ ions of 10^8 ions per second (equivalent to $1.67 \times 10^{-2} \text{ mol m}^{-2} \text{ s}^{-1}$) while effectively inhibiting the Cl[−] transport across the cell membrane (Fig. S1)²². When surface-charged nanochannels are immersed in the liquid electrolyte, an electrical double layer (EDL) will form, which includes a Helmholtz layer adjacent to the solid surface and a mobile layer extending into the liquid²³. Specifically,

the Helmholtz layer comprises an inner Helmholtz layer (IHP) and an outer Helmholtz layer (OHP). The characteristic screening length called Debye length λ_d refers to the total length of IHP and OHP, which can be determined by²⁴:

$$\lambda_d = \sqrt{\frac{\varepsilon_0 \varepsilon_r k T}{2 N_A e^2 I}} \quad (1)$$

Where ε_0 represents the vacuum dielectric constant, ε_r denotes the dielectric constant of the electrolyte, k stands for Boltzmann's constant, T is the temperature, N_A is the Avogadro's number, e is the elementary charge, and I is the ionic strength of the electrolyte. Ionic strength (I) is determined by C_0 according to its definition. In high-concentration electrolyte solution where the $\lambda_d \ll h$ (channel size), the characteristics in the channel feature bulk behavior. When the ionic strength is low, λ_d is comparable to or larger than h . The ion transport within the EDL region of nanochannels shows a distinct nanofluidic effect, resulting in nearly constant ionic conductance (K)²⁵. Ion transport behavior in such channels differs significantly from bulk behavior, showcasing both high ion selectivity and fast ion conduction simultaneously²⁶. The principle underlying nanofluidic ion transport is fundamental to biological ion channels and has found some applications in some specific fields such as osmotic energy harvesting and ion-regulating devices^{27–29}. Despite its significance, there are few reports on applying the principle to enhance the performance of LMEs.

Based on Sand's formula (Fig. 1) (more details are presented in Supplementary Note 1), a decrease in D and μ_+ will reduce the T_{sand} and thus promote the emergence of Li dendrites and dead Li³⁰. Although the implications of T_{sand} on ionic depletion are primarily applicable at length scales much larger than the typical interelectrode distance in metal batteries³¹, in this study, we just use the Equation of Sand's time to describe the effect of two parameters, Li⁺ diffusion coefficient (D) and Li⁺ transference number (μ_+), on Li deposition. Based on the above analysis, nanofluidic channels (NFCs) with an aligned structure are introduced to achieve selective and fast conduction of Li⁺. The electrolyte concentration on the electrode interface (C) continuously decreases during the Li plating, which leads to a decrease of I , facilitating the occurrence of nanofluidic effects and enabling fast and selective Li⁺ flow, thus preventing the emergence of Li dendrites and achieving uniform Li deposition.

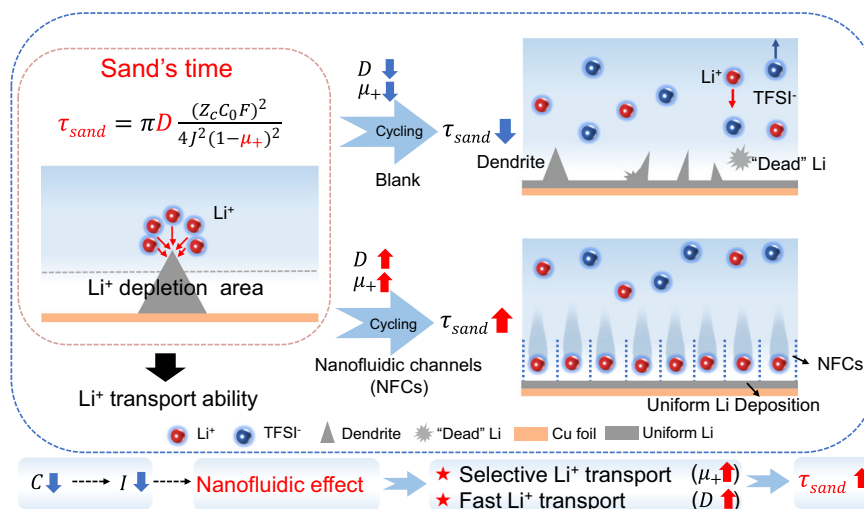


Fig. 1 | Bioinspired design of the artificial interphase layer for high Li⁺ selectivity and fast Li⁺ conduction. Schematic illustration showing the Li⁺ transport and Li plating on the interface of LMEs without and with the artificial interphase layer inspired by the nanofluidic effects (AIL-NFE).

Herein, as a proof of concept, we developed the AIL-NFE on LMEs using 4-carboxyl-quinoline linked covalent organic frameworks with NFCs to achieve enhanced D and μ_+ of Li^+ , aiming to construct high-rate dendrite-free LMEs. Owing to the unique nanofluidic effect within the AIL-NFE, its ionic conductivity remains high even at a low salt concentration ($\leq 10^{-4} \text{ mol L}^{-1}$ LiTFSI). The AIL-NFE facilitates selective and rapid conduction of Li^+ , exhibiting a D that is 10^7 times higher than that in bulk solution at a low salt concentration ($10^{-6} \text{ mol L}^{-1}$ LiTFSI). Simultaneously, the μ_+ of the AIL-NFE at the same salt concentration is 3.6 times higher than that of the bulk solution. The greatly enhanced D and μ_+ lead to improved Li^+ transport ability on the interface of Li metal and eventually enable the stable Li plating/stripping even at high current densities and low temperatures. As a result, the AIL-NFE functionalized LME achieves a stable Li plating/stripping cycling even at a high current density of 200 mA cm^{-2} and a high CE of 99.4% at -20°C . The negative electrode-free Cu||LFP cells based on the AIL-NFE demonstrate a capacity retention of 80.1% after 200 cycles. Furthermore, the efficacy of the AIL-NFE is demonstrated on a Li||S pouch cell (single-layer), which delivers a high specific energy of 505.1 Wh kg^{-1} , showcasing promising practical applications.

Results and discussion

The AIL-NFE exhibits high ion selectivity and fast ion conduction across the membrane. Two major factors influence the ion-transport properties of the AIL-NFE: (1) the channel size of the AIL-NFE and (2) the surface charge of the AIL-NFE. The λ_d in the electrolyte at different concentrations can be calculated by Eq. (1) (Fig. 2a). It can be obtained that the λ_d is 2.86 and 9.05 nm in 10^{-3} and $10^{-4} \text{ mol L}^{-1}$ LiTFSI solution, respectively (more details are shown in Table S1). The 4-carboxyl-quinoline-linked covalent organic frameworks were synthesized according to the one-pot Doebner reaction (Fig. S2)³². The powder X-ray diffraction (PXRD) spectra of the covalent organic frameworks reveal diffraction peaks at 2θ angles of 2.90° , 5.04° , 5.70° , and 7.82° , which correspond to (100), (110), (200) and (210) planes, respectively (Fig. S3)³². The formation of the 4-carboxyl-quinoline linkage within the covalent organic frameworks was confirmed using solid-state nuclear magnetic resonance (SSNMR) and Fourier transform infrared spectroscopy (FT-IR) (Figs. S4 and S5). Zeta potential analysis indicates a negative surface charge on the nanochannels, attributed to the presence of the carboxylic acid groups (Fig. S6). The nanometer-sized channels of the covalent organic frameworks were investigated using SAXS and nitrogen adsorption experiments at 77 K (Fig. S7). The average diameter of the channels was calculated ($h = 2\pi/q$) using the $q = 2.1 \text{ nm}^{-1}$ of the peak and determined to be $\sim 3 \text{ nm}$ (Fig. 2b). The interplanar d-spacing of 3.03 nm was confirmed using transmission electron microscopy (TEM) (Fig. S8), along with the corresponding fast Fourier transformation pattern (FFT), which matches the (100) lattice plane observed in the PXRD result ($2\theta = 2.90^\circ$).

The nanofluidic ion transport behavior of the synthesized AIL-NFE was investigated in a conventional ether electrolyte (LiTFSI in DOL/DME = 1/1 vol) (Fig. 2c) (more details are presented in Figs. S9 and S10)³³. Based on these conductances (the slope of the I-V curve), corresponding conductivity values could be calculated by Eq. (S1) (Fig. S9). It can be observed that the ionic conductivity (K) of the bulk solution is proportional to concentration due to the free migration of ions in the bulk solution. However, the K of the AIL-NFE membrane deviates from the lower trend of the bulk solution and shows a constant ionic conductivity at a concentration below $10^{-4} \text{ mol L}^{-1}$, displaying the typical nanofluidic ion transport behavior. Because the negatively-charged nanochannels are less than the λ_d (9.05 nm) in $10^{-4} \text{ mol L}^{-1}$ LiTFSI solution, the EDL region in the channels of the AIL-NFE overlap, resulting in a single and enriched Li^+ environment within the AIL-NFE. For a further investigation of nanofluidic ion transport applicable to practical batteries, the D at various LiTFSI concentrations was calculated based on the EIS measurements

according to Eq. (S9) (more details are presented in Fig. S11)³⁴. Notably, the Li^+ transport behaviors of the AIL-NFE exhibit two different characteristics. At high concentrations, the D linearly decreases and is close to the values of the bulk solution. At a concentration below $10^{-4} \text{ mol L}^{-1}$, the D of the AIL-NFE increases rapidly, displaying fast ion conduction behavior (Fig. 2d). The D of the AIL-NFE ($1.0 \times 10^{-10} \text{ cm}^2 \text{ s}^{-1}$ at $10^{-6} \text{ mol L}^{-1}$ LiTFSI) is significantly higher than that of the bulk electrolytes ($1.1 \times 10^{-17} \text{ cm}^2 \text{ s}^{-1}$ at $10^{-6} \text{ mol L}^{-1}$ LiTFSI) at low salt concentrations.

Furthermore, we also investigated the μ_+ of the AIL-NFE at different concentrations according to Eq. (S10) (more details are presented in Figs. S12 and S13)³⁴. Results show that the Li^+ selectivity of the AIL-NFE membrane is significantly higher than that of the bulk solution at low salt concentrations (below $10^{-4} \text{ mol L}^{-1}$), suggesting that AIL-NFE exhibits unique nanofluidic ion behavior (Fig. 2e). Meanwhile, the Li^+ permeability was quantitatively measured by constructing the AIL-NFE membrane between asymmetric chambers with different concentrations of LiTFSI solution. The I-V curve collected when the concentration ratio is 10 indicates a four-order preference for Li^+ over TFSI according to the Goldman-Hodgkin-Katz (GHK) equation (more details are presented in Fig. S14)³⁵. The results confirm the high Li^+ ion selectivity (4 times higher than that in bulk solution) and fast Li^+ ion diffusion (10^7 times higher than that in bulk solution) in the AIL-NFE at a low LiTFSI concentration ($10^{-6} \text{ mol L}^{-1}$) (Fig. 2f), which indicates a fast and selective Li^+ conduction at the interface of Li negative electrode when Li plating especially under high current densities.

To explore the Li^+ diffusion and Li plating behavior, a continuum model (COMSOL) is employed to simulate the Li^+ moving and concentration evolution. As Li deposition increases, the Li^+ concentration on the “tips” is higher than the near surface of the Li negative electrode. This creates “hot spots”, where Li^+ ions preferentially nucleate, leading to the formation and growth of Li dendrites (Figs. 2g and S15). The AIL-NFE with uniformly distributed NFCs facilitates fast and selective Li^+ conduction at the Li negative electrode interface, preventing the formation of Li^+ depletion zones and enabling uniform Li deposition (Figs. 2j and S15). The Li dendrites more easily emerge under a high current density (80 mA cm^{-2}) or a low temperature (-20°C) due to the easier occurrence of Li depletion zones (Figs. 2h, i and S16, S17). In contrast, the uniform Li deposition is still obtained for the AIL-NFE-covered LMEs at the same condition (Figs. 2k, l and S16, S17). Even in an electrolyte with a low LiTFSI concentration of $10^{-3} \text{ mol L}^{-1}$, the AIL-NFE-covered LME also shows stable and uniform Li plating (Fig. S18). Therefore, it is anticipated that high-rate dendrite-free LMBs will be constructed by utilizing the AIL-NFE.

The Li||Cu asymmetric cells and Li||Li symmetric cells were assembled to investigate the effect of the AIL-NFE on the electrode kinetics. The exchange current density of the LMEs is 1.39 and 0.43 mA cm^{-2} with and without the AIL-NFE, respectively, indicating enhanced Li^+ transfer kinetics in the presence of AIL-NFE (Fig. 3a)³⁶. The activation energy for Li deposition is 0.184 and 0.288 eV with and without the AIL-NFE, respectively, indicating that the AIL-NFE can promote the Li^+ transport and reduce the energy barrier for Li deposition (Figs. 3b and S19)³⁷. Additionally, Li deposition kinetics on the Li metal surface can also be investigated using cyclic voltammetry (CV). The pronounced redox peaks vary with various sweep rates (v) during voltammetry experiments and the relation is expressed as $i = av^b$ with the value of b providing insight into the Li^+ transport mechanism (Fig. S20). The b -value during Li^+ deposition is 0.91 and 0.48, respectively, with and without the AIL-NFE (Fig. 3c). The results reveal that the diffusion-limited process without the AIL-NFE is transformed into a surface-controlled process after introducing the AIL-NFE, indicating an adequate Li^+ ion source and fast Li^+ ion replenishment on the interface of LMEs upon plating due to the nanofluidic effect³⁸. Furthermore, the intrinsic current was also measured at different current densities from 20 to $120 \mu\text{A}$ and the intrinsic current (i_t) was calculated using Eq. (S12) (Figs. S21 and 3d). The i_t is calculated to

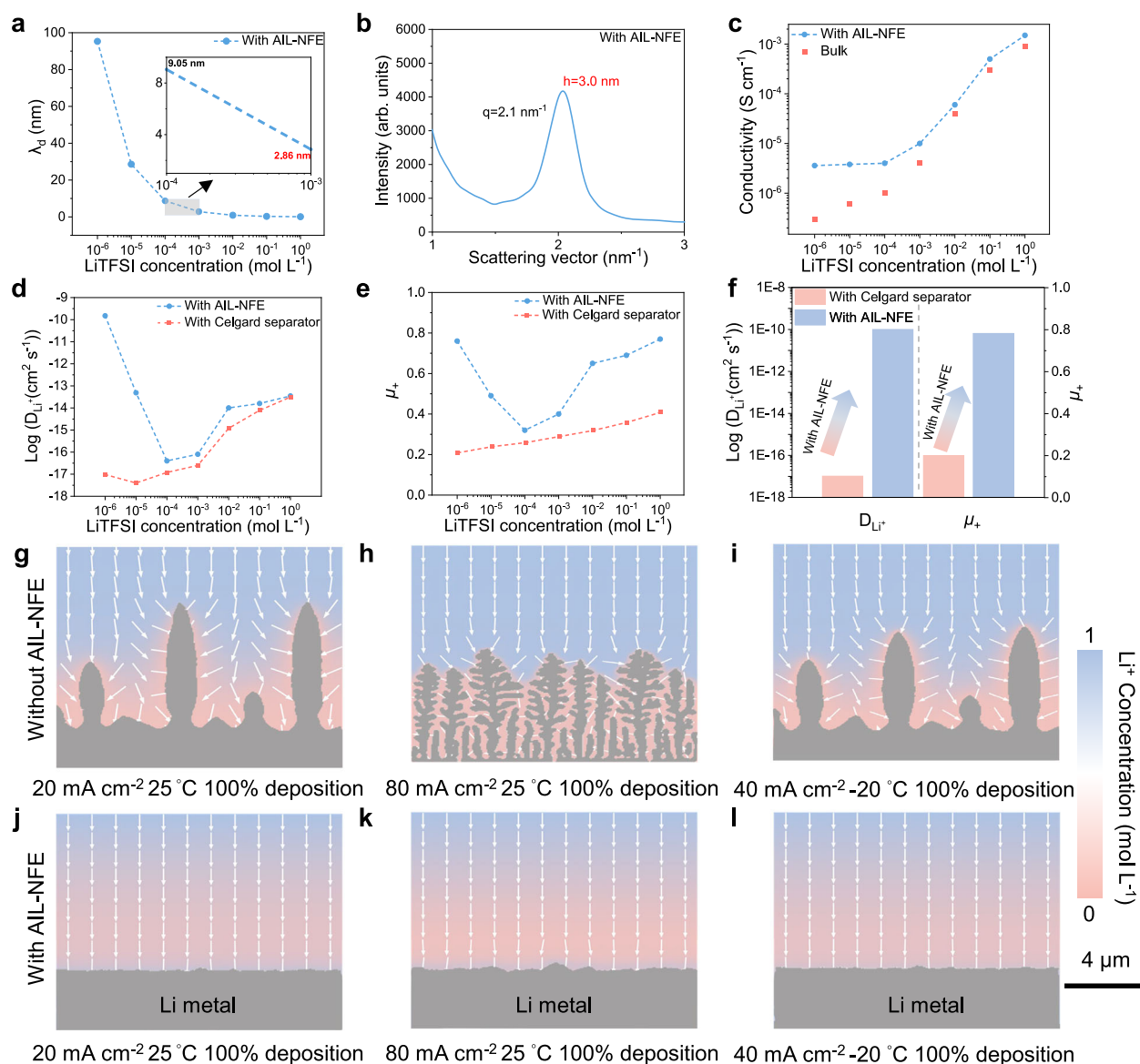


Fig. 2 | Mechanism exploration of the nanofluidic ion transport behavior.

a Debye length of the AIL-NFE in LiTFSI solutions with various concentrations. Inset is a partially enlarged view. **b** Small-angle X-ray scattering (SAXS) data showing the channel size of the AIL-NFE. **c** Ionic conductivities of the AIL-NFE in LiTFSI solutions with various concentrations. **d** Diffusion coefficient of Li^+ with and without the AIL-NFE in LiTFSI solutions with various concentrations. **e** Transference number of Li^+ with and without the AIL-NFE in LiTFSI solutions with various concentrations. **f** Comparison of the D and μ_+ with and without the AIL-NFE in a solution with a

LiTFSI concentration of $10^{-6} \text{ mol L}^{-1}$. Simulation of Li^+ ion concentration evolution in the electrolyte and Li dendrite growth during the Li plating process after 100% Li deposition (corresponding to $0.667 \text{ mAh cm}^{-2}$) without and with the AIL-NFE at different current densities and temperatures: **g, j** 20 mA cm^{-2} and 25°C ; **h, k** 80 mA cm^{-2} and 25°C ; **i, l** 40 mA cm^{-2} and -20°C . The color gradient in the visualization represents variations in the concentration of Li^+ , while the arrows depict the direction and magnitude of the Li^+ flux. Source data are provided as a Source Data file.

be 0.211 and 0.164 mA with and without AIL-NFE, respectively. The high i_r means that adequate Li^+ ions are on the surface for Li deposition due to the fast and selective Li^+ conduction³⁹.

The influence of the AIL-NFE on the morphology of Li deposition was monitored by scanning electrochemical microscopy (SECM). Ultramicroelectrodes (UMEs) are used to probe the electrochemical surface, providing information about morphological change at nanoscale levels (Fig. S22)⁴⁰. It is evident that after the Li deposition, the surface current signal of the LMEs with the AIL-NFE is more uniform compared to that of the LMEs without the AIL-NFE (Fig. 3e, f), reflecting a more even surface of LMEs. The interfacial charge transfer kinetics of the bare Cu and Cu@AIL-NFE electrodes were further investigated by the in-situ electrochemical impedance spectroscopy (EIS) combined with distribution of relaxation time (DRT) technique analysis

(Figs. S23 and 3g, h)⁴¹. The low-frequency region (0.1 – 100 s in the DRT plot) corresponds to the Warburg impedance arising from the Li^+ ion diffusion process⁴¹. As shown in Fig. 3g, h, the small intensity in the low-frequency region indicates low Warburg impedance and provides further evidence for the crucial role of the nanofluidic effects induced by the AIL-NFE, which contributes to the accelerated Li^+ transfer. In situ optical microscopy measurement was conducted to further investigate the efficacy of AIL-NFE for Li deposition. The Li negative electrode without the AIL-NFE exhibits a rough surface with a large amount of mossy Li dendrites (Fig. 3i). In contrast, the Li negative electrode with the AIL-NFE demonstrates a dendrite-free and flat surface structure. Additionally, the results of atomic force microscopy (AFM) further indicate that the surface morphology of the LMEs with the AIL-NFE is smoother and denser compared to that of the bare LMEs as plating

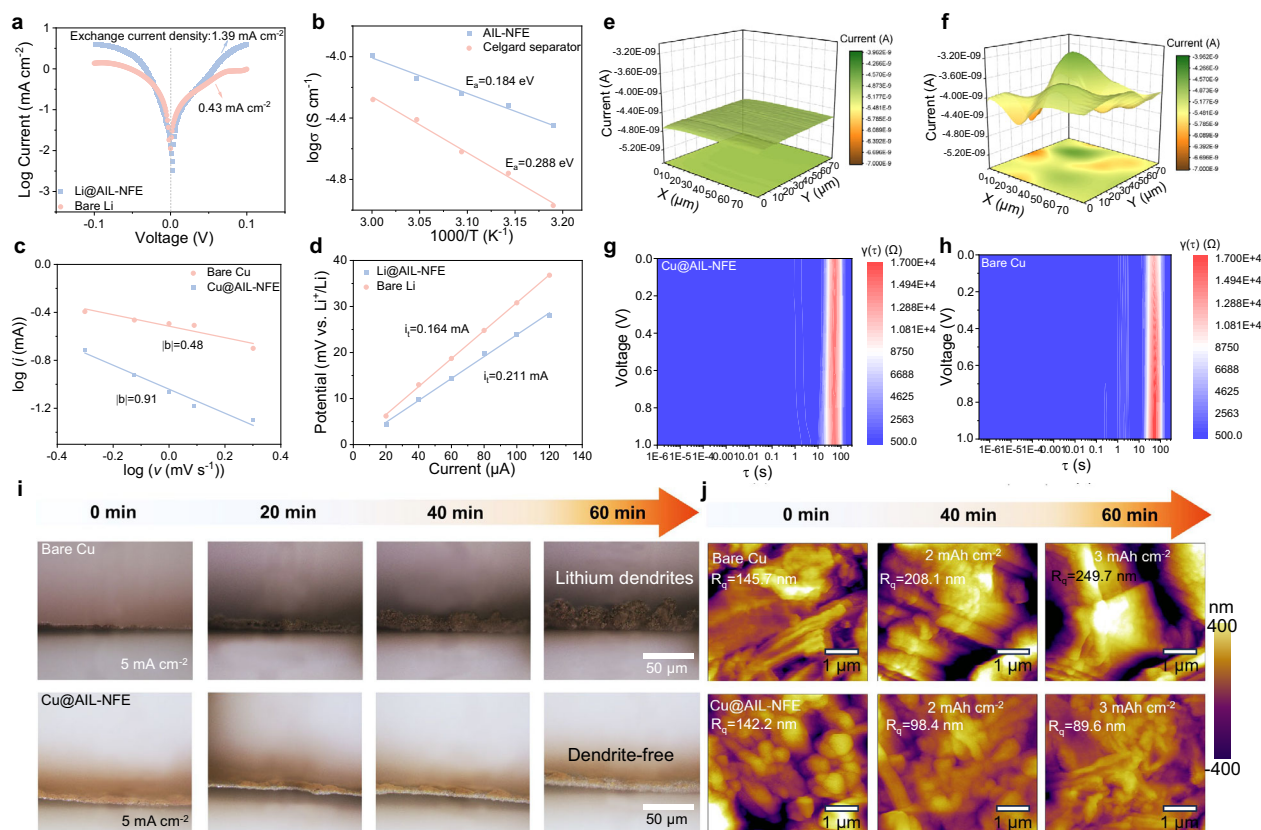


Fig. 3 | Electrochemical characterization of the effect of the AIL-NFE on the electrode kinetics. **a** Tafel and **b** apparent activation energy curves for the Li||Li cells based on the LMEs with and without the AIL-NFE. **c** Linear fitting of $\lg(i_a)$ (oxidative peak current) to $\lg(v)$ (sweep rate) from the CV curves with various sweep rates and **d** Intrinsic current of LMEs with and without the AIL-NFE. **e, f** Current

distribution images of LMEs on Cu foil after Li deposition with and without the AIL-NFE. **g, h** In situ DRT profiles derived from EIS data at the second cycle from 1.0–0.0 V. **i** In situ optical microscopy images and **j** AFM mapping images of Li electrodeposition without and with the AIL-NFE. Source data are provided as a Source Data file.

time increases, which can be evidenced by a smaller root mean square (RMS) value (Fig. 3j).

Achieving dendrite-free Li stripping and plating at high current densities is crucial for developing high-rate LMBs. A 5 mAh cm^{-2} Li layer was pre-deposited on a Cu foil at 1 mA cm^{-2} as the LMEs for subsequent cell testing. The SEM images display that the thickness of the AIL-NFE is about $5.2 \mu\text{m}$ and an even Li deposition layer ($10.0 \mu\text{m}$) is underneath the AIL-NFE (Fig. 4a, b). In contrast, uneven Li deposition of approximately $17.0 \mu\text{m}$ with numerous Li dendrites is observed on the bare Cu (Fig. 4c, d). As shown in Fig. 4e, the Li||Cu@AIL-NFE asymmetric cell demonstrates a high CE of 99.7% using the modified Aurbach method. The asymmetric Li||Cu cell without the AIL-NFE can only be stably operated for 75 cycles and the CE decreases subsequently (Figs. 4f and S24a). The Li||Cu@AIL-NFE asymmetric cell exhibits a prolonged cycle life of 200 cycles with a high average CE. The average CE of the Li||Cu@AIL-NFE asymmetric cell between 100 and 200 cycles can be as high as 99.0% (Fig. S24b). The time-of-flight secondary ion mass spectrometry (TOF-SIMS) analysis was conducted to characterize the content and distribution of the residual Li fragments on a Cu foil after finishing Li stripping. The results reveal that less metallic Li remains on the Cu foil with the AIL-NFE modification, indicating that it has higher reversibility of stripping and plating (Fig. 4g).

The rate performance of Li||Li symmetric cells with and without the AIL-NFE was investigated at a deposition capacity of 1 mAh cm^{-2} . The Li||Li symmetric cell with the AIL-NFE displays a stable polarization voltage at different current densities from 5 to 100 mA cm^{-2} , while the Li||Li symmetric cell without the AIL-NFE shows an increased and unstable polarization voltage (Fig. 4h, i). The structure and component

of the SEIs on the bare Cu and Cu@AIL-NFE were conducted by XPS with depth profiling and TOF-SIMS. The results indicate that the content of by-products such as Li_2CO_3 , LiO_3H_3 , and CH_3O^- in the SEI layer for the Cu@AIL-NFE is decreased (Figs. S25 and 4j), indicating the side reactions are suppressed and contributing to enhancing the reversibility. To further verify the effectiveness of AIL-NFE in improving the stability of LMEs, the long-term cycling performance of the Li||Li symmetric cell with the AIL-NFE is evaluated. As shown in Figs. 4k and S26, the Li||Li symmetric cell with the AIL-NFE can stably operate over 1000 h at a high current density of 50 mA cm^{-2} , while the Li||Li symmetric cell based on the bare Li metals only cycles for 40 h. Furthermore, the symmetric cells with the Li@AIL-NFE electrodes also display long cycling stability under different current densities and deposition capacities (Figs. S27–S31). Especially, the Li||Li symmetric cell with the AIL-NFE can cycle for more than 6500 h (equivalent to more than 9 months) with a current density of 5 mA cm^{-2} and maintain stable cycling for 100 h even at a high current density of 200 mA cm^{-2} (Fig. S31). SEM images of Li metal in the symmetric cells confirm that the use of AIL-NFE effectively inhibits the formation of Li dendrites (Figs. S32 and S33). Li^+ transport is slow at low temperatures, which more likely facilitates the growth of Li dendrites. As shown in Fig. 4l, the Li||Cu@AIL-NFE asymmetric cell still shows a high CE of 99.4% at 0.5 mA cm^{-2} and 0.5 mAh cm^{-2} under -20°C , which is much higher than that of the asymmetric Li||Cu cell without the AIL-NFE (95.1%). Furthermore, Li||Li symmetric cells were tested at -20°C . Over a cycling period extending to 200 h, the symmetric cell uses bare Li cycles for 200 h, and eventually, a short circuit occurs (Fig. S34). In contrast, the Li||Li symmetric cell with the AIL-NFE exhibits stable Li

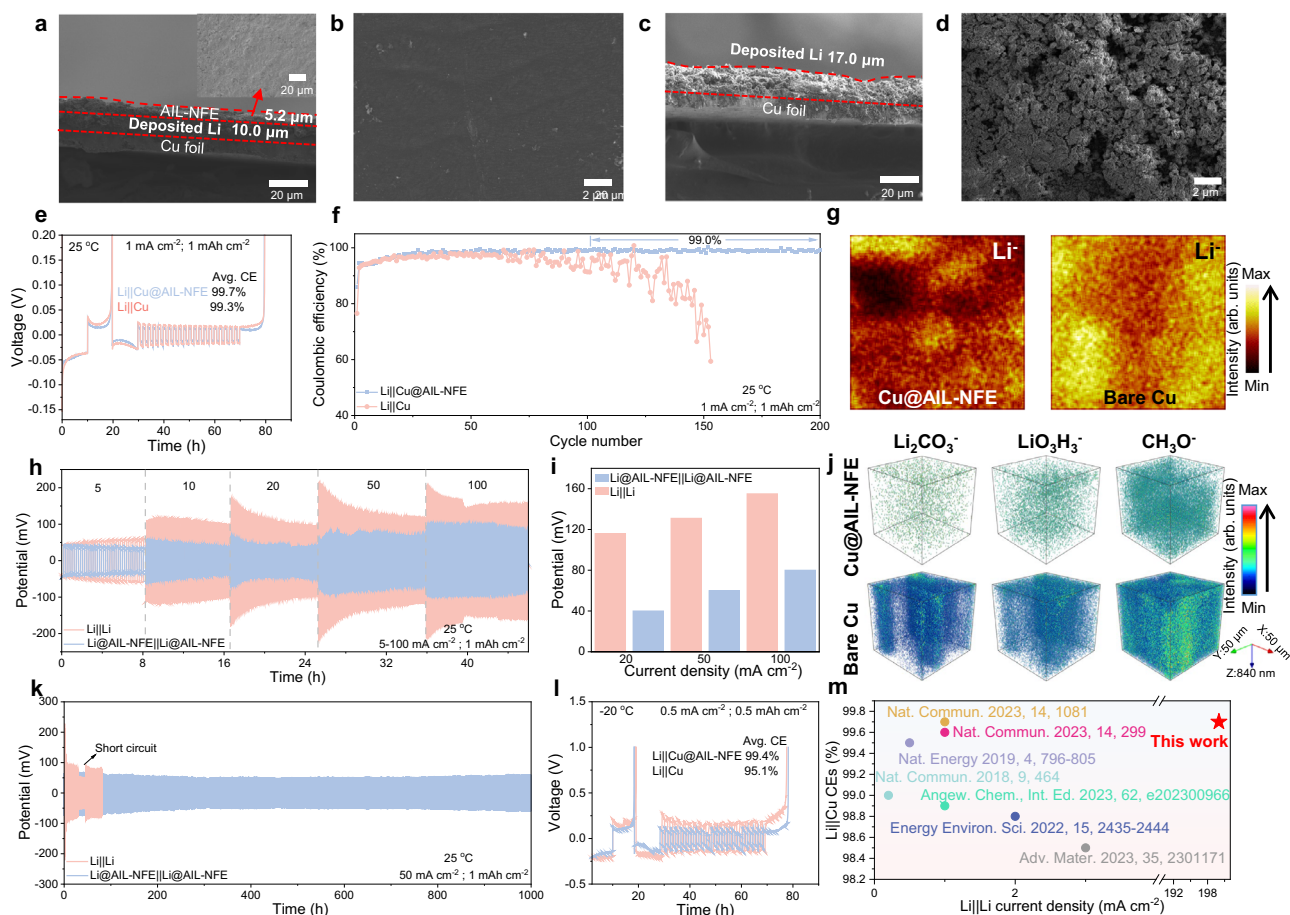


Fig. 4 | Electrochemical performance of Li negative electrode. **a** Cross-sectional SEM image of the electrodeposited Li on the Cu@AIL-NFE (Inset, top view of SEM image of the AIL-NFE on the Cu@AIL-NFE). **b** SEM image showing the surface of the electrodeposited Li on the Cu@AIL-NFE after peeling the AIL-NFE. **c** Cross-sectional SEM image of the electrodeposited Li on the bare Cu. **d** SEM image showing the surface of the electrodeposited Li on the bare Cu. **e** Voltage profiles versus time of the asymmetric Li||Cu and Li||Cu@AIL-NFE cells using the modified Aurbach method (25 °C). **f** CE of the asymmetric Li||Cu and Li||Cu@AIL-NFE cells (1 mA cm⁻²; 1 mAh cm⁻²). **g** 2D TOF-SIMS images showing the Li⁺ fragments on the Cu@AIL-NFE and bare Cu after finishing stripping. **h** Rate performance of the Li||Li symmetric cells with the bare Li and Li@AIL-NFE from 5 to 100 mA cm⁻² (areal capacity: 1 mAh cm⁻²). **i** Comparison of polarization voltage of the Li||Li symmetric cells with the bare Li and Li@AIL-NFE. **j** 3D TOF-SIMS sputtering images of selected secondary ion fragments of Li₂CO₃⁻, LiO₃H₃⁻, and CH₃O⁻ on the cycled Cu@AIL-NFE (after peeling the AIL-NFE) and bare Cu. **k** Long-term cycling stability of symmetric cells (50 mA cm⁻²; 1 mAh cm⁻²). **l** Voltage profiles versus time of the asymmetric Li||Cu and Li||Cu@AIL-NFE cells using the modified Aurbach method (-20 °C). **m** Performance comparison of our Li@AIL-NFE electrode with other state-of-the-art Li electrodes (The source of the literature data shown in this figure can be found in Supplementary Information, Table S2). Source data are provided as a Source Data file.

plating and stripping for 700 h at -20 °C. SEM images of Li metal in the symmetric cell with bare Li reveal powdered Li and dendrite formation (Fig. S35). In contrast, the Li||Li symmetric cell with the AIL-NFE shows Li metal surfaces with uniform and flat Li deposition. Based on the findings, the near-surface Li⁺ ions of the bare Li are depleted during Li deposition and are slow to replenish due to sluggish Li⁺ diffusion, particularly under high current densities, creating Li⁺ depletion zones. Consequently, Li deposition primarily occurs at electrode surface tips due to the “tip effect”, leading to the formation of Li dendrites and “dead” Li. In contrast, the AIL-NFE facilitates rapid and selective Li⁺ conduction at the Li negative electrode interface, preventing the formation of Li⁺ depletion zones and ensuring uniform and stable Li deposition. As a result, when the AIL-NFE is employed in LMEs, it significantly enhances CE and enables operation at high current densities (Fig. 4m)^{42–48}.

The electrochemical performances of the assembled Li||LFP and Li||S batteries based on the bare Li and Li@AIL-NFE were investigated. As displayed in Fig. 5a, the LFP cell with bare Li experiences a short circuit after 510 cycles at 2 C. In contrast, the LFP cell with the Li@AIL-NFE negative electrode exhibits high-capacity retention, retaining

88.7% of its initial capacity after 1000 cycles at 2 C. The rate performance of LFP full cells assembled with the Li@AIL-NFE also surpasses that of those using bare Li (Fig. 5b). At a current density of 0.5 C and with 20.1 mg cm⁻² LFP loading, an LFP full cell with the Li@AIL-NFE was tested, demonstrating an initial capacity of 141.9 mAh g⁻¹, maintaining a high capacity retention of 95.5% after 200 cycles (Fig. 5c). Negative electrode-free LFP cells with high LFP loadings of 13.1 and 28.1 mg cm⁻² were further assembled to verify the efficacy of AIL-NFE. The negative electrode-free LFP cells with LFP loadings of 13.1 and 28.1 mg cm⁻² demonstrate high capacity retention of 80.1% after 200 cycles at 0.3 C (Figs. 5d and S36) and 90.6% after 60 cycles at 0.1 C, respectively (Fig. S37). These results exceed some of previous related findings on negative electrode-free LFP cell (Fig. 5e and Table S3)^{49–55}. Furthermore, we integrated a pressure sensing system to monitor pressure changes in the Li||LFP pouch cells throughout cycling, aiming to assess the effectiveness of the AIL-NFE in promoting uniform lithium deposition (Fig. S38). Throughout the cycle, the pressure variation of the Li||LFP pouch cells with the AIL-NFE remains lower compared to cells with bare Cu, and the pressure is close to the initial pressure after the discharge (Fig. 5f). Figure 5g shows the pressure maps of the

1 mAh cm⁻². **i** Comparison of polarization voltage of the Li||Li symmetric cells with the bare Li and Li@AIL-NFE. **j** 3D TOF-SIMS sputtering images of selected secondary ion fragments of Li₂CO₃⁻, LiO₃H₃⁻, and CH₃O⁻ on the cycled Cu@AIL-NFE (after peeling the AIL-NFE) and bare Cu. **k** Long-term cycling stability of symmetric cells (50 mA cm⁻²; 1 mAh cm⁻²). **l** Voltage profiles versus time of the asymmetric Li||Cu and Li||Cu@AIL-NFE cells using the modified Aurbach method (-20 °C). **m** Performance comparison of our Li@AIL-NFE electrode with other state-of-the-art Li electrodes (The source of the literature data shown in this figure can be found in Supplementary Information, Table S2). Source data are provided as a Source Data file.

88.7% of its initial capacity after 1000 cycles at 2 C. The rate performance of LFP full cells assembled with the Li@AIL-NFE also surpasses that of those using bare Li (Fig. 5b). At a current density of 0.5 C and with 20.1 mg cm⁻² LFP loading, an LFP full cell with the Li@AIL-NFE was tested, demonstrating an initial capacity of 141.9 mAh g⁻¹, maintaining a high capacity retention of 95.5% after 200 cycles (Fig. 5c). Negative electrode-free LFP cells with high LFP loadings of 13.1 and 28.1 mg cm⁻² were further assembled to verify the efficacy of AIL-NFE. The negative electrode-free LFP cells with LFP loadings of 13.1 and 28.1 mg cm⁻² demonstrate high capacity retention of 80.1% after 200 cycles at 0.3 C (Figs. 5d and S36) and 90.6% after 60 cycles at 0.1 C, respectively (Fig. S37). These results exceed some of previous related findings on negative electrode-free LFP cell (Fig. 5e and Table S3)^{49–55}. Furthermore, we integrated a pressure sensing system to monitor pressure changes in the Li||LFP pouch cells throughout cycling, aiming to assess the effectiveness of the AIL-NFE in promoting uniform lithium deposition (Fig. S38). Throughout the cycle, the pressure variation of the Li||LFP pouch cells with the AIL-NFE remains lower compared to cells with bare Cu, and the pressure is close to the initial pressure after the discharge (Fig. 5f). Figure 5g shows the pressure maps of the

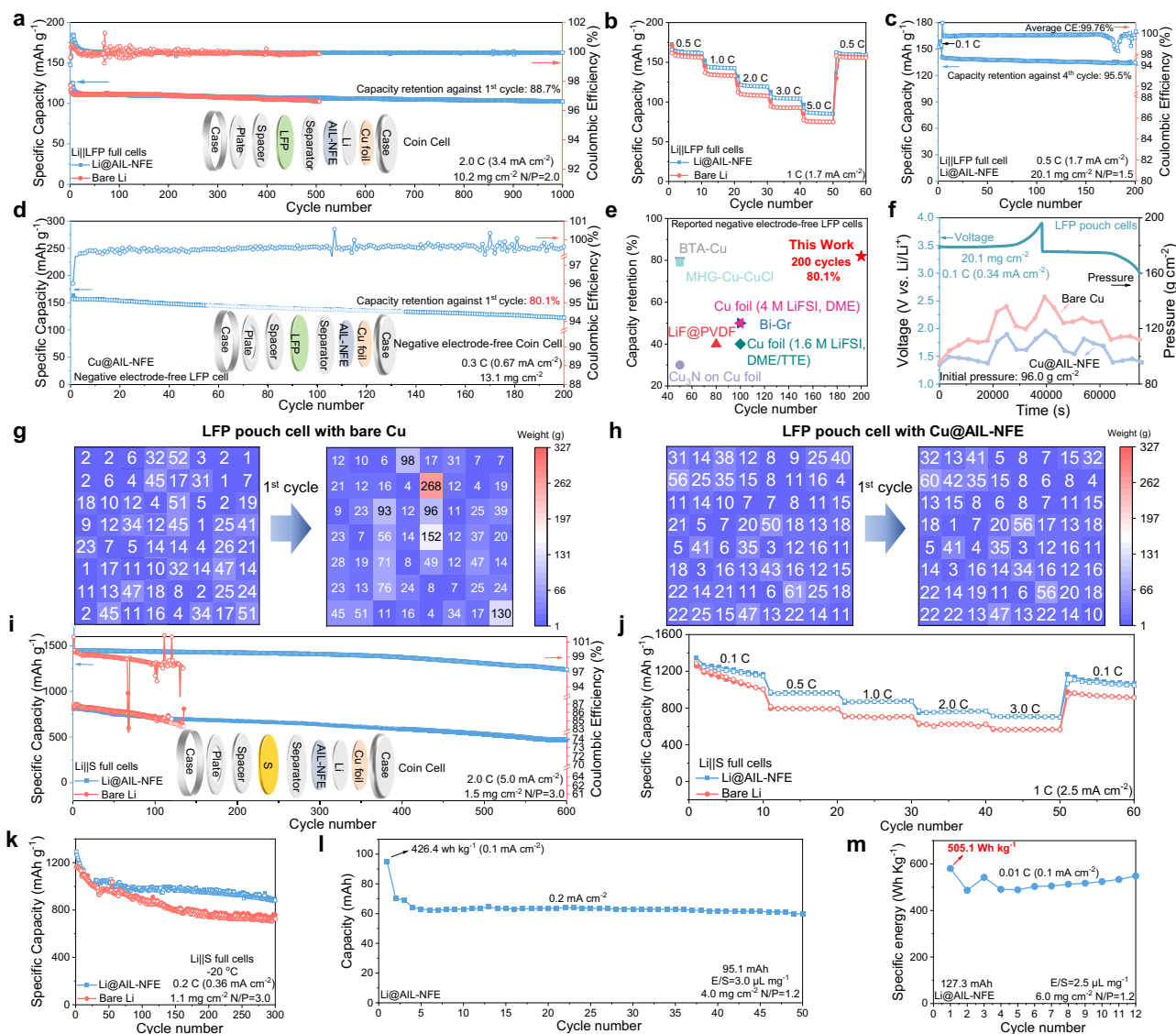


Fig. 5 | Electrochemical performance of the Li||LFP and Li||S batteries. a Long-term charge and discharge cycling of the Li||LFP cells with the bare Li and Li@AIL-NFE at 2 C. **b** Rate performance of Li||LFP cells with the bare Li and Li@AIL-NFE. **c** Cycling performance of Li||LFP cell based on the Li@AIL-NFE with an LFP loading of 20.1 mg cm⁻² at 0.5 C. **d** Cycling performance of the negative electrode-free LFP cell with the Cu@AIL-NFE. **e** Comparison of cycling performance of our negative electrode-free LFP cell based on the Cu@AIL-NFE with other reported work. The source of the literature data shown in this figure can be found in Supplementary Information, Table S3. **f** Pressure variation diagrams for the LFP pouch cells with the bare Cu and Cu@AIL-NFE during the first cycle. Pressure distribution maps of the

LFP pouch cell with bare Cu (**g**) and Cu@AIL-NFE (**h**) before and after the first cycle. The number of each pixel represents the weight existing at that position (the areal is 0.0625 cm², unit (g)). **i** Long-term charge and discharge cycling of Li||S cells with the bare Li and Li@AIL-NFE at 2 C. **j** Rate performance of Li||S cells with the bare Li and Li@AIL-NFE. **k** Cycling performance of the Li||S cells with the bare Li and Li@AIL-NFE at -20 °C. **l** Cycling performance of Li||S pouch cells based on the Li@AIL-NFE negative electrode with an S loading of 4.0 mg cm⁻² (S loading: 64 mg). **m** Energy density of Li||S pouch cells based on the Li@AIL-NFE negative electrode with an S loading of 6.0 mg cm⁻² (S loading: 96 mg). Source data are provided as a Source Data file.

Li||LFP pouch cell with the bare Cu after the first cycle, large pressure values of 268 g (equivalent to 4288 g cm⁻²) are observed in certain regions, indicating uneven lithium deposition. In contrast, the pressure maps show that the pouch cell with the AIL-NFE shows uniform pressure distribution after cycling, confirming the homogeneous lithium deposition during the cycle (Fig. 5h).

The Li||S cell utilizing bare Li encounters short circuits after 130 cycles at a high rate of 2 C, likely due to insufficient Li⁺ ion supply and Li corrosion induced by the shuttle effect (Fig. 5i). In contrast, the Li||S cell with the Li@AIL-NFE demonstrates prolonged cycling stability, maintaining a high specific capacity of 510.6 mAh g⁻¹ even after 600 cycles at 2 C. SEM images of the cycled negative electrode, along with corresponding S element mappings on the Li negative electrodes, are

illustrated in Fig. S39. The surface of bare Li shows an uneven and porous structure, accompanied by a large amount of sulfur distribution. In contrast, the cycled Li@AIL-NFE surface exhibits a dendrite-free and dense morphology with minimal sulfur distribution. These findings indicate that rapid Li⁺ ion transport induced by the nanofluidic effect effectively prevents Li dendrite growth, while the AIL-NFE prevents contact between polysulfides and the Li surface, thereby suppressing the passivation and corrosion of LMEs. Figure 5j illustrates the rate performance of Li||S cells assembled with bare Li and Li@AIL-NFE. The Li||S cells with the Li@AIL-NFE exhibit enhanced rate performance (Fig. S40a), achieving specific capacities of 716.6 mAh g⁻¹ at 3 C, whereas the Li||S cells with the bare Li displays lower specific capacities, reaching only 563.4 mAh g⁻¹ at 3 C (Fig. S40b). The rate

performance of the Li||S cells assembled with Li@AIL-NFE exceeds some of previous related findings on Li||S cells (Fig. S41 and Table S4). Furthermore, the Li||S cell with the Li@AIL-NFE also delivers a high initial areal capacity of 4.5 mAh cm^{-2} under a high S loading (5.0 mg cm^{-2}) (Fig. S42). The AIL-NFE can not only improve the performance of LMEs at high current densities but also address the limitations of Li^+ transport kinetics at low temperatures by the nanofluidic effects. Figure S43 shows the average temperature distribution map of China in Jan. 2024, revealing that 38% of the area experiences temperatures below -20°C and 83% of the area experiences temperatures below 0°C . Therefore, enhancing the low-temperature performance of batteries is of great significance. As shown in Fig. 5k, the cycling stability of the Li||S cell with the Li@AIL-NFE at -20°C outperforms that of the cell with bare Li. These results underscore the efficacy of AIL-NFE functionalization in achieving high-rate and low-temperature The source of the literature data batteries.

A Li||S pouch cell (single-layer) was fabricated using the Li@AIL-NFE and an S electrode with a loading of 4.0 mg cm^{-2} (E/S ratio: $3 \mu\text{L mg}^{-1}$) to assess the effectiveness of the AIL-NFE in practical operation (Fig. S44). The assembled Li-S pouch cell achieves a notable specific capacity of $1278.9 \text{ mAh g}^{-1}$ at 0.20 mA cm^{-2} even after 50 cycles (Fig. 5l; additional details in Table S5). To further enhance high energy density, a practical cell with a higher S loading of 6.0 mg cm^{-2} , low N/P ratio (1.2) and E/S ratio ($2.5 \mu\text{L mg}^{-1}$) was assembled using the AIL-NFE to show its efficacy in high-specific-energy devices. The weight distribution of components in this Li-S pouch cell (single-layer) with the Li@AIL-NFE was quantified, and the energy density was calculated (Fig. S45). The assembled Li||S pouch cell achieves a high initial energy density of 505.1 Wh kg^{-1} at 0.01C and successfully powers a display device (Fig. 5m; additional details in Fig. S46 and Table S6).

In summary, the AIL-NFE with aligned NFCs was developed to greatly enhance the D and μ_+ on the interface of the Li negative electrode, thus enabling high-rate and dendrite-free LMEs. The AIL-NFE enables a high ionic conductivity in a conventional ether electrolyte (DOL: DME = 1:1 vol%) even at a low concentration below $10^{-4} \text{ mol L}^{-1}$, displaying the typical nanofluidic ion transport behavior, which benefits a high μ_+ (0.77 at $10^{-6} \text{ mol L}^{-1}$ LiTFSI) and D ($1.0 \times 10^{-10} \text{ cm}^2 \text{ s}^{-1}$ at $10^{-6} \text{ mol L}^{-1}$ LiTFSI). The selective and rapid conduction of Li^+ ions effectively suppress the growth of Li dendrites, thereby enabling stable cycling of Li||Li symmetric cells incorporating the Li@AIL-NFE even at high current densities of 200 mA cm^{-2} and a high CE of 99.7% at 25°C . When implemented in LMBs, the negative electrode-free LFP cell demonstrates a high capacity retention of 80.1% after 200 cycles at 0.3 C. Moreover, the resulting Li||S pouch cell based on the Li@AIL-NFE can be stably cycled for 300 cycles with a high capacity retention of 70.7% even under -20°C and achieve a high initial energy density of 505.1 Wh kg^{-1} at 0.01 C, showing the efficacy of the AIL-NFE in high-energy devices. The nanofluidic effect-inspired artificial interfacial layer presented in this study offers a promising strategy for realizing high-rate and high-energy-density LMBs.

Methods

Materials

Multiwalled carbon nanotubes (CNTs, >99.5%) were purchased from Nanjing Xianfeng Nano Co. Ltd (Jiangsu, China). Sulfur was purchased from Shanghai Adamas-beta Reagent Co., p-phthalaldehyde, 1,3,5-TPB, o-dichlorobenzene, n-butyl alcohol, n-propyl alcohol, and glacial acetic acid were purchased from TENSUS BIOTECH (shanghai, China). All chemicals were analytical grade and used without further purification. The copper foil (thickness: $10 \mu\text{m}$), aluminum foil (thickness: $16 \mu\text{m}$), Carbon black (Super P), LFP particles, Celgard 2500, 2032-type coin-cell cases, springs, and spacers and metallic Li foil (thickness: $50 \mu\text{m}$, $450 \mu\text{m}$, Li content $\geq 99.9\%$) were obtained from Canrd Technology Co. Ltd. The electrolyte (1M

Lithium bis(trifluoromethanesulfonyl)imide (LiTFSI) in DOL/DME = 1/1 vol with 2 wt% LiNO_3 addition), polyvinylidene difluoride (PVDF 5130, Mw = 1,300,000), LA132 (MA-EN-BI-0015, Mw = 450,000) and N-methylpyrrolidone (NMP, >99.0%) were obtained from Dodo-Chem. All solvents were stored over 4 \AA molecular sieves for 72 h before use. All of the electrolytes were prepared in a glove box filled with argon gas ($\text{O}_2 < 0.01 \text{ ppm}$, $\text{H}_2\text{O} < 0.01 \text{ ppm}$).

Synthesis of 4-carboxyl-quinoline linked covalent organic frameworks

A 10 mL Schlenk tube was used to combine p-phthalaldehyde (96.6 mg, 0.72 mmol), 1,3,5-TPB (168 mg, 0.48 mmol), o-dichlorobenzene (3.0 mL), n-butyl alcohol (3.0 mL), and glacial acetic acid ($200 \mu\text{L}$). The mixture was sonicated for 20 min before adding pyruvic acid ($100 \mu\text{L}$, 1.44 mmol) with vigorous vortexing. The tube was then subjected to a degassing-filling cycle using a Schlenk line in a liquid N_2 bath at 77 K and sealed. The reaction mixture was heated at 120°C for 72 h, resulting in a precipitate. This precipitate was collected by suction filtration, washed three times with n-hexane (15 mL), ethyl acetate (30 mL), and methanol (30 mL), and then dried in a vacuum oven at 60°C for 12 h.

Fabrication of AIL-NFE membrane and Cu@AIL-NFE

For the preparation of AIL-NFE membrane or Cu@AIL-NFE, 80 mg 4-carboxyl-quinoline linked covalent organic frameworks, 10 mg PVDF was dissolved into NMP solvent to generate a homogenous solution. The mixture was then vigorously stirred for 12 h at room temperature. The prepared dispersion was then coated onto an aluminum foil or Cu foil using a spread coating method and dried under 100°C to obtain the AIL-NFE membrane or Cu@AIL-NFE.

Preparation of sulfur and LFP positive electrodes

Sulfur and LFP positive electrodes were achieved using a slurry casting method. 80 wt% CNT/sulfur composite or LFP powder, 10 wt% Super-P, and 10 wt% LA132 binder were mixed in n-propyl alcohol to form a slurry and then coated on aluminum current collectors using a doctor blade coater (MSK-NFA-III, Hefei Kejing Materials Technology Co., Ltd) and dried at 55°C in a vacuum oven for 24 h. The electrode sheets were then cut to the corresponding size (diameter: 12 mm) using a battery slitter (MSK-520, SHENZHEN KEJING STAR TECHNOLOGY COMPANY).

Materials characterizations

The X-ray powder diffraction patterns of the covalent organic frameworks were tested on a Bruker D8 Advance diffractometer at 40 kV and 40 mA with a Cu target tube and a graphite monochromator. The structure and morphology were characterized by field-emission scanning electron microscopy (SEM) (TESCAN Brno, s.r.o. MAIA3). X-ray photoelectron spectrometry (PerkinElmer PHI 1600 ESCA) was carried out to identify the surface chemical composition of the SEI film. The pore-size distribution of the covalent organic frameworks was obtained by N_2 adsorption/desorption isotherm (Belsorp-max). The spectroscopic characteristics of the covalent organic frameworks were revealed with Fourier transform infrared spectroscopy (FTIR, Thermo Scientific NICOLET IS50). Scanning electrochemical microscopy (SECM) tests were performed on the CHI920D Electrochemical workstation (Chenhua, Shanghai). The Zeta potential at room temperature was determined using the Malvern Zetasizer Nano ZS90 testing machine. The morphology of Li electrodeposition was determined using an atomic force microscope (AFM, Bruker Dimension Icon). The procedures for the preparation of the electrode samples were conducted in a glove box filled with argon gas ($\text{O}_2 < 0.01 \text{ ppm}$, $\text{H}_2\text{O} < 0.01 \text{ ppm}$) at $25 \pm 5^\circ\text{C}$, and the samples were sealed in an argon atmosphere without exposure to air during the transfer process.

Simulations of Li metal deposition and Li⁺ distribution

The simulations are conducted to investigate the Li metal deposition and Li⁺ distribution, using COMSOL Multiphysics 6.1 in this work. The simulations are performed with phase field and electrodeposition model. In the phase field model, the variable ϕ is defined in the range from 0 to 1. While “ $\phi = 1$ ” and “ $\phi = 0$ ” represent the Li phase and electrolyte phase, respectively. Initially, the govern region is set as the electrolyte phase. During calculation, the variable with the values “ $0 < \phi < 1$ ” will occur at the interface of two phases, which represents the transitional phase. The ion flux was governed by the Nernst-Planck equation. The reaction is described using the Butler-Volmer equation. In the simulation, the introduction of covalent organic frameworks determines the diffusion of Li⁺ in the electrolyte, which is given in the experiments and affects the depositions of Li metals. 20%, 60%, and 100% Li deposition correspond to 0.133, 0.400 and 0.667 mAh cm⁻², respectively.

Electrochemical measurements

2032 type coin cells were assembled in a glove box filled with argon gas (O₂ < 0.01 ppm, H₂O < 0.01 ppm). The symmetric Li|Li and asymmetric Li|Cu cells with and without AIL-NFE coating were assembled. A 5 mAh cm⁻² Li was first pre-deposited on a Cu foil (diameter: 14 mm) with or without the AIL-NFE at a current density of 1 mA cm⁻² for typical cell tests. For Li|Li symmetric cell with the AIL-NFE coating at a current density of 50 mA cm⁻² (areal capacity: 5 mAh cm⁻²), a 10 mAh cm⁻² Li (thickness: 50 μm) was first pre-deposited on a Cu foil (diameter: 14 mm) with the AIL-NFE at a current density of 1 mA cm⁻² for cell test. CR2032 coin cells were employed and assembled in an argon-filled glove box using the as-prepared CNT/S positive electrodes or LFP positive electrodes, separator, and modified Li metal negative electrode (Case and spring material: stainless steel). The electrolyte for battery tests is 1 M Lithium bis(trifluoromethanesulfonyl)imide (LiTFSI) in DOL/DME = 1/1 vol with 2 wt% LiNO₃ addition. A commercial Celgard 2500 (thickness: 25 μm; porosity: 55%; average pore size: 0.064 μm) was used as the separator (diameter: 19 mm). Galvanostatic discharge/charge curves, rate, and cycling performance of Li|S cells were tested by a LAND CT2001A instrument with a voltage window between 1.6–2.8 V at 30 ± 5 °C in a climatic chamber. The coin cells were sealed by a manual battery hydraulic sealer sealing machine with a pressure of 700 psi. For each Li|S cell, the electrolyte/sulfur (E/S) usage ratio is controlled at around 5 μL mg⁻¹ for a typical electrode. Cyclic voltammograms (CV) curves of Li|S cells were obtained by using an electrochemical workstation at a scan rate of 0.1 mV s⁻¹ between 1.6–2.8 V. Galvanostatic discharge/charge curves, rate and cycling performance of Li|LFP cells were tested by LAND CT2001A instrument with the voltage window between 2.8–3.9 V, and the electrolyte amount was controlled to be 50 μL. The EIS test and Li⁺ ion migration number were measured in Li|Li symmetric batteries with a frequency range from 1 MHz to 0.01 Hz and an amplitude of 5 mV (potentiostatic, Steps/Decade = 10, quasi-stationary potential). The Li|Cu cells were assembled to test the efficiency of Li deposition and stripping for different negative electrodes in the voltage range of 0–1.0 V. For the negative electrode-free LFP cell, to minimize the initial Li consumption during the formation of the SEI layer, the Cu@AIL-NFE was pretreated by plating/stripping for 3 cycles at 1.0 mA cm⁻² for 1.0 mAh cm⁻². The deposited Li was completely stripped to 1.0 V in the final step and thus was assumed that no active Li remained in the pretreated Cu@AIL-NFE. For the Li|S pouch cell (single layer) with an S loading of 4.0 mg cm⁻² (positive electrode area: 4.0 × 4.0 cm²), the Li@AIL-NFE (area: 4.0 × 4.0 cm²) with an areal capacity of 7.0 mAh cm⁻² and Celgard 2500 (area: 4.0 × 4.0 cm²) were used as the negative electrode and separator, respectively. 0.19 mL electrolyte (E/S = 3 μL mg⁻¹) was then injected into the pouch cell. For the Li|S pouch cell (single layer) with an S loading of 6.0 mg cm⁻² (positive electrode area: 4.0 × 4.0 cm²), The Li@AIL-NFE (area: 4.0 × 4.0 cm²) with an areal capacity of 10.0 mAh cm⁻² and

Celgard 2500 (area: 4.0 × 4.0 cm²) were used as the negative electrode and separator, respectively. 0.24 mL electrolyte (E/S = 2.5 μL mg⁻¹) was then injected into the pouch cell. For all pouch cells, an 86 μm aluminum plastic film for the external packaging. The pouch cell was vacuum sealed at 180 °C under −90 kPa. The pouch cell was tested with an initial pressure of about 100 kPa with a dew point below −60 °C at a temperature of 30 ± 5 °C. Scanning electrochemical microscope (SECM) tests were performed on the CHI920D Electrochemical workstation (Chenhua, Shanghai, China). The CH116 microprobe and Cu electrodes were used as the first and second working electrodes, Li foil was used as the reference electrode, and the platinum wire electrode was assembled into a four-electrode system. The working solution is 10 mM 2,5-ditertbutyl-1,4-dimethoxybenzene (DBDMB) + 1 M LiTFSI in DOL/DME = 1/1 vol, in which DBDMB was used as the redox medium. For the pressure study, the M1616S sensor (Crownto, China) was used for pressure sensing with a maximum sensing area of 5.5 × 5.5 cm², a minimum pressure sensing limit of >10 g cm⁻², and the 2D pressure sensor has 256 nodes for an area of 4.0 × 4.0 cm², and thus, the areal sensing resolution is 0.0625 cm². The sensor with a maximum sensing speed of 30 Hz and M1616S software was used for pressure calibration and mapping analysis. A pressure sensor was attached to a pouch cell and placed between the compression plates. Pressure variation diagrams for the LFP pouch cells are based on the average pressure of all 256 nodes, and the pressure distribution map of the LFP pouch cell is based on 64 nodes in the central area. Pressure values were recorded at intervals of 1 s. For the assembly of the LFP pouch cells (4.0 × 4.0 cm² in area), The mass loading of LFP is 20.1 mg cm⁻² (positive electrode area: 4.0 × 4.0 cm²), Celgard2500 (thickness: 25 μm; porosity: 55%; average pore size: 0.064 μm, area: 4.0 × 4.0 cm²) and the negative electrode capacity (negative electrode area: 4.0 × 4.0 cm²) to positive electrode capacity ratio (N/P ratio) is fixed at 1.5. Electrolyte (E/C = 3.0 μL mg⁻¹) was then injected into the pouch cell.

Data availability

All data needed to evaluate the conclusions in the paper are present in the paper and/or the Supplementary Information. Source data are provided with this paper.

References

1. Yu, X. & Manthiram, A. A progress report on metal–sulfur batteries. *Adv. Funct. Mater.* **30**, 2004084 (2020).
2. Chen, Y. et al. Advances in lithium–sulfur batteries: from academic research to commercial viability. *Adv. Mater.* **33**, 2003666 (2021).
3. Yang, X., Luo, J. & Sun, X. Towards high-performance solid-state Li–S batteries: from fundamental understanding to engineering design. *Chem. Soc. Rev.* **49**, 2140–2195 (2020).
4. Song, C.-L. et al. Single-atom zinc and anionic framework as janus separator coatings for efficient inhibition of lithium dendrites and shuttle effect. *ACS Nano* **15**, 13436–13443 (2021).
5. Li, Y. et al. An artificial interfacial layer with biomimetic ionic channels towards highly stable Li metal anodes. *Sci. Bull.* **68**, 1379–1388 (2023).
6. Liang, X. et al. A facile surface chemistry route to a stabilized lithium metal anode. *Nat. Energy* **2**, 17119 (2017).
7. He, G., Li, Q., Shen, Y. & Ding, Y. Flexible amalgam film enables stable lithium metal anodes with high capacities. *Angew. Chem. Int. Ed.* **58**, 18466–18470 (2019).
8. Shen, X. et al. Lithium–matrix composite anode protected by a solid electrolyte layer for stable lithium metal batteries. *J. Energy Chem.* **37**, 29–34 (2019).
9. Jin, S. et al. Solid–solution-based metal alloy phase for highly reversible lithium metal anode. *J. Am. Chem. Soc.* **142**, 8818–8826 (2020).
10. Wang, Q. et al. Advanced electrolyte design for stable lithium metal anode: from liquid to solid. *Nano Energy* **80**, 105516 (2021).

11. Jiang, G. et al. Robust artificial solid-electrolyte interfaces with biomimetic ionic channels for dendrite-free Li metal anodes. *Adv. Energy Mater.* **11**, 2003496 (2021).
12. Lin, Y. et al. Constructing a uniform lithium iodide layer for stabilizing lithium metal anode. *J. Energy Chem.* **55**, 129–135 (2021).
13. Chen, X.-R., Zhao, B.-C., Yan, C. & Zhang, Q. Review on Li deposition in working batteries: from nucleation to early growth. *Adv. Mater.* **33**, 2004128 (2021).
14. Bai, P., Li, J., Brushett, F. R. & Bazant, M. Z. Transition of lithium growth mechanisms in liquid electrolytes. *Energy Environ. Sci.* **9**, 3221–3229 (2016).
15. Wang, Q. et al. Li⁺ migration and transformation at the interface: a review for stable Li metal anode. *Energy Storage Mater.* **55**, 782–807 (2023).
16. Wang, S. et al. Nanoscale observation of the solid electrolyte interface and lithium dendrite nucleation–growth process during the initial lithium electrodeposition. *J. Mater. Chem. A* **8**, 18348–18357 (2020).
17. Xu, R. et al. Unlocking the polarization and reversibility limitations for stable low-temperature lithium metal anodes. *Small Struct.* **4**, 2200400 (2023).
18. Du, J. et al. Mitigating concentration polarization through acid–base interaction effects for long-cycling lithium metal anodes. *Nano Lett.* **23**, 3369–3376 (2023).
19. Xiao, Z. et al. Eliminating concentration polarization with gradient lithiophilic sites towards high performance lithium metal anodes under low N/P ratio. *Chem. Eng. J.* **480**, 148029 (2024).
20. Zhang, X., Antonietti, M. & Jiang, L. Bioinformation transformation: from ionics to quantum ionics. *Sci. China Mater.* **63**, 167–171 (2020).
21. Song, B. & Jiang, L. The macroscopic quantum state of ion channels: a carrier of neural information. *Sci. China Mater.* **64**, 2572–2579 (2021).
22. Zhang, X., Liu, H. & Jiang, L. Wettability and applications of nano-channels. *Adv. Mater.* **31**, 1804508 (2019).
23. Chen, G. et al. A highly conductive cationic wood membrane. *Adv. Funct. Mater.* **29**, 1902772 (2019).
24. Chen, C. & Hu, L. Nanoscale ion regulation in wood-based structures and their device applications. *Adv. Mater.* **33**, 2002890 (2021).
25. Li, T. et al. A nanofluidic ion regulation membrane with aligned cellulose nanofibers. *Sci. Adv.* **5**, eaau4238 (2019).
26. Zhang, H. et al. Ultrafast selective transport of alkali metal ions in metal organic frameworks with subnanometer pores. *Sci. Adv.* **4**, eaq0066 (2018).
27. Li, X. et al. Fast and selective fluoride ion conduction in sub-1-nanometer metal-organic framework channels. *Nat. Commun.* **10**, 2490 (2019).
28. Hou, S. et al. Charged porous asymmetric membrane for enhancing salinity gradient energy conversion. *Nano Energy* **79**, 105509 (2021).
29. Tang, J. et al. All-natural 2D nanofluidics as highly-efficient osmotic energy generators. *Nat. Commun.* **15**, 3649 (2024).
30. Cai, Y. et al. An ionic liquid electrolyte with enhanced Li⁺ transport ability enables stable Li deposition for high-performance Li–O₂ batteries. *Angew. Chem. Int. Ed.* **60**, 25973–25980 (2021).
31. Mistry, A. et al. Electrolyte confinement alters lithium electrodeposition. *ACS Energy Lett.* **4**, 156–162 (2019).
32. Yang, Y. et al. Constructing chemical stable 4-carboxyl-quinoline linked covalent organic frameworks via doebner reaction for nanofiltration. *Nat. Commun.* **13**, 2615 (2022).
33. Si, L. et al. A superstable, flexible, and scalable nanofluidic ion regulation composite membrane. *Sci. Bull.* **68**, 2344–2353 (2023).
34. Nie, L. et al. Integration of porous high-loading electrode and gel polymer electrolyte for high-performance quasi-solid-state battery. *Adv. Energy Mater.* **14**, 2302476 (2024).
35. Pan, Y. et al. Introducing ion-transport-regulating nanochannels to lithium-sulfur batteries. *Nano Energy* **33**, 205–212 (2017).
36. Yang, Y. et al. Hydrogen-bonded organic framework as superior separator with high lithium affinity C=N bond for low N/P ratio lithium metal batteries. *Nano Lett.* **23**, 5061–5069 (2023).
37. Whiteley, J. M. et al. FeS₂-imbedded mixed conducting matrix as a solid battery cathode. *Adv. Energy Mater.* **6**, 1600495 (2016).
38. Simon, P., Gogotsi, Y. & Dunn, B. Where do batteries end and supercapacitors begin? *Science* **343**, 1210–1211 (2014).
39. Guo, Y. et al. An autotransferable g-C₃N₄ Li⁺-modulating layer toward stable lithium anodes. *Adv. Mater.* **31**, 1900342 (2019).
40. Mahankali, K., Thangavel, N. K. & Reddy Arava, L. M. In situ electrochemical mapping of lithium–sulfur battery interfaces using AFM–SECM. *Nano Lett.* **19**, 5229–5236 (2019).
41. Wang, H. et al. Accelerating sulfur redox kinetics by electronic modulation and drifting effects of pre-lithiation electrocatalysts. *Adv. Mater.* **36**, 2307741 (2024).
42. Zhang, G. et al. A monofluoride ether-based electrolyte solution for fast-charging and low-temperature non-aqueous lithium metal batteries. *Nat. Commun.* **14**, 1081 (2023).
43. Zhao, Y., Zhou, T., Mensi, M., Choi, J. W. & Coskun, A. Electrolyte engineering via ether solvent fluorination for developing stable non-aqueous lithium metal batteries. *Nat. Commun.* **14**, 299 (2023).
44. Cao, X. et al. Monolithic solid–electrolyte interphases formed in fluorinated orthoformate-based electrolytes minimize Li depletion and pulverization. *Nat. Energy* **4**, 796–805 (2019).
45. Zou, P. et al. Directing lateral growth of lithium dendrites in micro-compartmented anode arrays for safe lithium metal batteries. *Nat. Commun.* **9**, 464 (2018).
46. Piao, Z. et al. Stable operation of lithium metal batteries with aggressive cathode chemistries at 4.9 V. *Angew. Chem. Int. Ed.* **62**, e202300966 (2023).
47. Xiao, P. et al. A nonflammable electrolyte for ultrahigh-voltage (4.8 V-class) Li||NCM811 cells with a wide temperature range of 100 °C. *Energy Environ. Sci.* **15**, 2435–2444 (2022).
48. Su, H. et al. Achieving practical high-energy-density lithium-metal batteries by a dual-anion regulated electrolyte. *Adv. Mater.* **35**, 2301171 (2023).
49. Li, Q. et al. Homogeneous interface conductivity for lithium dendrite-free anode. *ACS Energy Lett.* **3**, 2259–2266 (2018).
50. Kang, T. et al. Dendrite-free lithium anodes enabled by a commonly used copper antirusting agent. *ACS Appl. Mater. Interfaces* **12**, 8168–8175 (2020).
51. Li, Z. et al. Gradient nano-recipes to guide lithium deposition in a tunable reservoir for anode-free batteries. *Energy Storage Mater.* **45**, 40–47 (2022).
52. Tamwattana, O. et al. High-dielectric polymer coating for uniform lithium deposition in anode-free lithium batteries. *ACS Energy Lett.* **6**, 4416–4425 (2021).
53. Shin, W. & Manthiram, A. A facile potential hold method for fostering an inorganic solid-electrolyte interphase for anode-free lithium-metal batteries. *Angew. Chem. Int. Ed.* **61**, e202115909 (2022).
54. Chen, J. et al. Electrolyte design for Li metal-free Li batteries. *Mater. Today* **39**, 118–126 (2020).
55. Qian, J. et al. Anode-free rechargeable lithium metal batteries. *Adv. Funct. Mater.* **26**, 7094–7102 (2016).

Acknowledgements

This work is supported by the Major Research Plan of the National Natural Science Foundation of China (92372207) (J.L.), National Natural Science Foundation of China (52302261) (Y.L.), the Guangdong Basic and Applied Basic Research Foundation (2023B1515120069 and 2024A1515012705) (Y.L.), Shenzhen Science and Technology Plan Project (No. SGDX20230116091644003) (Y.L.), high level of special funds

(G03034K001) (Y.L.), Guangdong Major Project of Basic and Applied Basic Research (2023B0303000002) (Y.L.), the Department of Mechanical and Energy Engineering-Jiahua Chemicals. Inc. Joint Lab Program, the Postdoctoral Fellowship Program of CPSF under Grant Number (GZC20240635) (C.S.).

Author contributions

Y.L., J.L., and T.Z. conceived and directed the project. Y.L. and C.S. proposed the concept and designed the experiments. C.S. prepared the materials and performed the electrochemical measurements. L.P. conducted the MD simulations. C.S., J.W. and L.C. performed the XPS measurements. C.S. and H.Z. instructed on the AFM testing. C.S., L.Y., and H.P. instructed on the SECM testing. C.S., S.W., and Y.J. instructed on the SEM testing. All authors contributed to the discussion and data analysis. C.S., J.L., and Y.L. wrote the manuscript, and all authors contributed to editing the manuscript.

Competing interests

The authors declare no competing interests.

Additional information

Supplementary information The online version contains supplementary material available at <https://doi.org/10.1038/s41467-025-62992-4>.

Correspondence and requests for materials should be addressed to Yiju Li, Jun Lu or Tianshou Zhao.

Peer review information *Nature Communications* thanks Changhong Cao, Yue Zhou and the other, anonymous, reviewer(s) for their contribution to the peer review of this work. [A peer review file is available].

Reprints and permissions information is available at <http://www.nature.com/reprints>

Publisher's note Springer Nature remains neutral with regard to jurisdictional claims in published maps and institutional affiliations.

Open Access This article is licensed under a Creative Commons Attribution-NonCommercial-NoDerivatives 4.0 International License, which permits any non-commercial use, sharing, distribution and reproduction in any medium or format, as long as you give appropriate credit to the original author(s) and the source, provide a link to the Creative Commons licence, and indicate if you modified the licensed material. You do not have permission under this licence to share adapted material derived from this article or parts of it. The images or other third party material in this article are included in the article's Creative Commons licence, unless indicated otherwise in a credit line to the material. If material is not included in the article's Creative Commons licence and your intended use is not permitted by statutory regulation or exceeds the permitted use, you will need to obtain permission directly from the copyright holder. To view a copy of this licence, visit <http://creativecommons.org/licenses/by-nc-nd/4.0/>.

© The Author(s) 2025